WILEY-VCH

DOI: 10.1002/ ((please add manuscript number))
Article type: Full Paper

Electrolytes Toward High-voltage $Na_3V_2(PO_4)_2F_3$ Positive Electrode Durable Against Temperature Variation

*Jinkwang Hwang, Kazuhiko Matsumoto,** and *Rika Hagiwara*

Dr. J. Hwang, Prof. K. Matsumoto, Prof. R. Hagiwara
Graduate School of Energy Science, Kyoto University
Yoshida-honmachi, Sakyo-ku, Kyoto 606-8501, Japan
E-mail: k-matsumoto@energy.kyoto-u.ac.jp

Prof. K. Matsumoto, Prof. R. Hagiwara
Unit of Elements Strategy Initiative for Catalysts & Batteries (ESICB), Kyoto University
Katsura, Kyoto 615-8510, Japan

The ORCID identification number(s) for the author(s) of this article can be found under https://doi.org/10.1002/
J. Hwang: 0000-0003-4800-3158
K. Matsumoto: 0000-0002-0770-9210
R. Hagiwara: 0000-0002-7234-3980

Keywords: sodium secondary batteries; electrolytes; $Na_3V_2(PO_4)_2F_3$; wide operating temperature; ionic liquids

High power and energy density, long cyclability, and tolerance for wide temperature (seasonal and daily operational temperature differences) must be considered to construct large-scale sodium secondary batteries. In this regard, $Na_3V_2(PO_4)_2F_3$ (NVPF) has become a subject of interest as a high-performance positive electrode material owing to its high energy density. However, the high operating voltage of NVPF causes continuous decomposition of electrolytes during cycles, resulting in significant capacity fading and low Coulombic efficiency. In this study, the electrochemical performance of the NVPF electrode in organic solvent electrolytes with and without VC and FEC additives and an ionic liquid is investigated at high voltage regimes over a wide temperature range (–20 °C to 90 °C). Our results reveal that the performance of organic electrolytes is still insufficient even with additives, and the ionic liquid electrolyte demonstrates high electrochemical stability and cyclability with NVPF electrodes in the temperature range from –20 °C to 90 °C, achieving stable cycling over 500 cycles. Detailed electrochemical analysis combined with X-ray photoelectron and energy dispersive X-ray spectroscopy indicates that a sturdy cathode electrolyte interphase layer around the electrode protects it from capacity fading at high voltage and elevated temperature, resulting in high Coulombic efficiency.

1. Introduction

The heightened awareness of sustainable energy production and socially responsible consumption has prompted a dynamic shift of focus into energy storage systems (ESS), notably, secondary battery technologies in recent years. Lithium secondary battery technology has taken center stage in many industrial and consumer applications, largely due to their unparalleled energy and power densities, great versatility and durability.[1, 2] Despite this, scarcity of lithium reserves, the high costs, and safety issues have been huge impediments to the advancement of this technology, forcing energy scientists to look into alternative solutions to this energy crisis.[3] Subsequently, rekindled interests into the advancement of sodium secondary batteries have emerged, owing to the abundance of natural sodium resources, their remarkable performance, low costs, and high energy densities.[2, 4-8] Although their success is greatly inhibited by the discovery and implementation of new electrode and electrolyte materials that can endure high temperatures and high voltage regimes operation.

As standard batteries are used in applications such as portable devices, electric vehicles, and intermittent energy supply stations, tolerance against massive climatic and operational temperature fluctuations is essential. **Figure 1a** shows the operating temperature range for the daily-use of secondary batteries classified by applications.[9] Until now, elevated temperatures have been a drawback to battery operations as they shorten battery lifespan, increase cooling costs and create safety problems. However, according to recent studies for some electrode materials and electrolytes, elevated temperatures improve ion mobility leading to superior rate capability and enhanced battery performance. Moreover, it enables the utilization of waste heat and boosts overall energy efficiency.[9-15] Thus, it would be expedient to identify novel battery components that would thrive in elevated temperatures.

For positive electrodes, polyanionic frameworks and layered transition-metal oxides

have been widely explored and integrated into sodium secondary batteries for their superior electrochemical performance resulting in an improved specific capacity.[6-20] Among which, vanadium-based phosphate fluoride (often mistaken with "fluorophosphate" despite the absence of P–F bond) such as $Na_3V_2(PO_4)_2F_3$ (NVPF) has attracted attention for its high potential two-step redox plateaus of 3.7 and 4.2 V (vs. Na^+/Na), the high theoretical capacity of 128 mAh g^{-1} and high specific energy density of ~450 Wh (kg^{-1} (vs. Na metal negative electrode).[21-26]

Although NVPF shows great potential as a future positive electrode material, it has intrinsically low electronic conductivity (10^{-12} S cm^{-1}) and demonstrates insufficient Coulombic efficiency, making it difficult to utilize its full capabilities. Furthermore, electrolytes that sustain its high temperature and high voltage regimes without disintegration remain scarce.[18] Extensive studies have yielded small improvements in the Coulombic efficiency and cyclability of NVPF through material modifications such as carbon coating, element doping, inserting conductive material, and electrolyte modifications (see **Table S1**) in attempts to boost its practicality.[24-42] Nonetheless, the identification of feasible electrolyte materials remains the most promising route to improve NVPF performance.

During the initial charge-discharge cycles of sodium secondary batteries, sodium ions migrate back and forth from the positive electrode to the negative electrode. This movement generates reactions on the electrode, causing partial degradation of the electrolyte. The degraded material is deposited on the electrode forming a thin passivation layer known as the solid electrolyte interface (SEI). The SEI protects the electrode from further reaction with the electrolyte while permitting the movement of Na^+ into the electrode. As such, an ideal SEI should be thin and impervious to electrolyte chemical components to improve battery efficiency, safety and to sustain long-term battery performance. Since sodium and lithium

secondary batteries have similarities in operation chemistries, previous studies have proposed swapping lithium electrolytes for sodium analogs. However, sodium cations have milder acidity compared to lithium cations and thus tend to form inhomogeneous and fragile SEI layers with higher solubility.[7, 11, 43-49] This allows further surface reactions between the electrode and electrolyte that induce further degradation and extra gas evolution that may create safety problems.[40, 50] For this reason, optimization of sodium electrolytes is a vital step towards the realization of high performance, safe and durable sodium secondary batteries.

The cathode electrolyte interface (CEI) layer, first confirmed by Thomas *et al.* on $LiCoO_2$ that exhibits high voltage[51] is formed on the positive electrode with characteristics akin to the SEI. Studies on CEI for lithium-ion batteries have shown that the CEI becomes less stable during high voltage operations.[52, 53] It could, therefore, be inferred that the large initial irreversible capacity observed on NVPF using conventional organic solvent electrolytes would form an unstable CEI layer accompanied by continuous electrolyte decomposition at high voltage. Therefore, the formation and stability of CEI, or lack of thereof, is a big stumbling block for high-voltage sodium secondary battery performance. (see Figure 1b). In an attempt to tackle this issue, a few studies on possible improvements have been conducted. Ponrouch *et al.* confirmed that the addition of DMC solvent (1 mol dm^{-3} $Na[ClO_4]$-$EC_{0.45}/PC_{0.45}/DMC_{0.1}$) improves the Coulombic efficiency of 98.5%.[39] Yan *et al*. revealed that adding DMC or the combination of four additives (vinylene carbonate (VC), succinonitrile, 1,3-propane sultone, and sodium difluoro(oxalate)borate) into 1 mol dm^{-3} $Na[PF_6]$-EC/PC stabilized cell performance at 55 °C.[43] (Table S1).

In this study, the basic electrochemical properties of eleven different sodium secondary battery electrolytes; Na[FSA], $Na[ClO_4]$, $Na[PF_6]$ in PC and in EC/DMC solvents with and without VC and FEC additives, and an ionic liquid of Na[FSA]-$[C_3C_1pyrr][FSA]$ (FSA =

bis(fluorosulfonyl)amide, PC = propylene carbonate, EC = ethylene carbonate, DMC = dimethyl carbonate, FEC = fluoroethylene carbonate, and C_3C_1pyrr = *N*-methyl-*N*-propylpyrrolidinium) were investigated at temperatures ranging from 25 °C to 60 °C, in order to compare their performance as electrolytes for the carbon-coated NVPF composite (NVPF-C) electrode. The Na[FSA]-[C_3C_1pyrr][FSA] ionic liquid showed the best performance in the basic electrochemical tests. For this reason, additional electrochemical performance tests that included rate capability, cyclability, and electrochemical impedance spectroscopy (EIS) combined with X-ray photoelectron (XPS) and energy dispersive X-ray (EDX) spectroscopy were performed in the extended temperature range of –20 °C to 90 °C, to clarify the effects of CEI layer on capacity fading and Coulombic efficiency.

2. Results and Discussion

2.1 Electrochemical Stability Based on Operating Temperatures.

Although it is a general understanding that the electrochemical stability window of electrolytes can be established through the computation of the energy difference between the highest occupied molecular orbital (HOMO) and lowest unoccupied molecular orbitals (LUMO) electronic structure theory,[54] previous studies have shown that the HOMO-LUMO energy gap is often an inaccurate representation of electrolyte stability. Electrolyte stability is much more multifaceted, as it is dependent on other factors such as the reactions between the solvent and salts within the electrolyte, concentrations, electrode materials, electrode surface states, temperatures, etc.[7, 54] For this reason, to assess the electrochemical stability of the electrolyte samples, linear sweep voltammetry (LSV) was performed on Al and C electrodes in two-electrode cells alongside a Na metal counter electrode (**Figures S1** and **S2**) and the electrolyte samples at variant temperatures of 25 °C, 45 °C, and 60 °C. The oxidative potential limits

(anode limits) of the electrolytes are summarized in **Figure 2.** The results reveal that at 25 °C, the Al electrodes (threshold: 0.01 mA cm^{-2}) exhibit oxidative potential limits of above 5.5V in 1 mol dm^{-3} Na[FSA]-[C_3C_1pyrr][FSA], 1 mol dm^{-3} Na[PF_6]-EC/DMC, and 1 mol dm^{-3} Na[PF_6]-PC. For 1 mol dm^{-3} Na[ClO_4]-PC, the Al electrodes demonstrate oxidative limits of above 4.7 V at the same temperature. At elevated temperatures of 45 °C and 60 °C, the wide oxidative potential limit appears to be preserved for 1 mol dm^{-3} Na[FSA]-[C_3C_1pyrr][FSA], but significantly narrowed for all organic solvent electrolytes as irreversible oxidative decomposition of the electrolytes occurred above 4 V. This radical decline in performance with the change in temperature explains the necessity of additives for the practical utilization of organic electrolytes. This behavior is further illustrated by the charge-discharge of NVPF-C at elevated temperature, as highlighted in the charge-discharge results below.

As shown in **Figure S3,** the SEM images and EDX mapping conducted on the Al electrodes following the LSV tests reveal severe pitting corrosion of electrodes anodically scanned in the 1 mol dm^{-3} and the 2 mol dm^{-3} Na[FSA]-PC and -EC/DMC electrolytes. This demonstrates that Al electrodes degrade irrespective of the Na[FSA] concentration or the solvents used to create the electrolytes (Figure S3a-d). The EDX mapping results indicate the presence of O, F, and S besides Al on the surface, suggesting the native oxide passivation layer on Al dissolves because the surface reacts with electrolytes (Figure S3a-d). The F and S elements detected by EDX suggest that the decomposition of FSA^- is involved in the corrosion process. For the Al electrode scanned in 1 mol dm^{-3} Na[ClO_4]-PC and -EC/DMC electrolytes, only light corrosion is observed (see Figure S3e,f). However, no corrosion is detected for 1 mol dm^{-3} Na[PF_6]-PC and EC/DMC, and Na[FSA]-[C_3C_1pyrr][FSA] as SEM images and EDX mapping illustrate elemental composition identical to that of a pristine Al electrode (Figure S3g-j).

Al metal is commonly used as a current collector for a positive electrode owing to high anodic stability created by the resilient layer of Al_2O_3 on the surface.[55-57] However, the passivation layer on Al seems to have deteriorated at regimes of above ~4 V in the 1 mol dm^{-3} and the 2 mol dm^{-3} Na[FSA]-PC and EC/DMC electrolytes, in concordance with results reported in a previous study.[58] This explicitly confirms that Na[FSA]-based organic electrolytes are not suitable for batteries that utilize Al current collectors. As such, only the electrolytes; 1 mol dm^{-3} Na[ClO_4]-PC, 1 Na[PF_6]-EC/DMC, and 1 mol dm^{-3} Na[FSA]-[C_3C_1pyrr][FSA] were selected for further electrochemical tests with a C electrode.

The anodic limits for each of the selected electrolytes; 1 mol dm^{-3} Na[ClO_4]-PC, 1 Na[PF_6]-EC/DMC, and 1 mol dm^{-3} Na[FSA]-[C_3C_1pyrr][FSA], was further evaluated by performing LSV on C electrodes in the electrolyte samples as summarized in Figure 2b and illustrated by LSV in Figure S2. In this set of experiments, acetylene black (AB) composite electrodes with poly(vinylidene fluoride) (PVDF) binder were used because of its large active surface area that provides a more suitable model of an actual battery electrode. Amongst the organic electrolytes, 1 mol dm^{-3} Na[PF_6]-EC/DMC demonstrates the best stability with the Al electrode. Therefore, it was selected to examine the effects of additives on electrolyte stability. 3 wt% FEC and 3 wt% VC were separately added into 1 mol dm^{-3} Na[PF_6]-EC/DMC to create new electrolyte samples, 1 mol dm^{-3} Na[PF_6]-EC/DMC + 3 wt% FEC and 1 mol dm^{-3} Na[PF_6]-EC/DMC + 3 wt% VC, respectively.

As observed in the LSV results, 1 mol dm^{-3} Na[PF_6]-EC/DMC and Na[ClO_4]-PC demonstrate significantly high anodic currents even at 25°C. The current densities increase with increasing temperatures as shown in Figure S2a,b, indicating decreasing electrolyte stability (oxidative potential limit) with an increase in temperature. The addition of FEC and VC additives into 1 mol dm^{-3} Na[PF_6]-EC/DMC was fairly effective in suppressing the anodic

current at all the temperatures (Figure S2c,d), indicating that the addition of additives has a positive effect on the electrolyte stability. The lowest anodic current is observed for 1 mol dm^{-3} Na[FSA]-[C_3C_1pyrr][FSA] regardless of the temperature changes (Figure S2e), corroborating the stability of the ionic liquid, 1 mol dm^{-3} Na[FSA]-[C_3C_1pyrr][FSA]. These results indicate that the choice of the electrolyte and the use of additives positively influence the oxidative stability of a positive electrode (for instance, NVPF-C as will be discussed in the following section). Moreover, the ionic liquid electrolyte establishes its capability to harness maximum electrochemical performance from a high-voltage positive electrode material in a wide temperature range.

2.2 Electrochemical Performance

2.2.1 Charge-discharge Behavior of NVPF-C

Details regarding the preparation and structural characteristics of NVPF-C can be found in the Additional Results and Discussion section, **Tables S2**–**S4**, and **Figures S4**–**S7** in Supporting Information.

Charge-discharge tests were performed on cells with NVPF-C electrodes against sodium metal negative electrodes immersed in the electrolyte samples and corresponding charge-discharge curves of their first were plotted as shown in **Figure 3** and **Figure S8**. The charging step of the cells continues over the preset time limit of 50 h. The charge-discharge curves for cells with 1 mol dm^{-3} and 2 mol dm^{-3} Na[FSA] in PC and EC/DMC (Figure S8 a-d) and the corresponding differential capacity vs. voltage plots (dQ/dV) shown in **Figure S9** are consistent with the LSV measurements that indicate irreversible oxidation begins around 4 V, (Figure 2a). Cells containing the 1 mol dm^{-3} Na[ClO_4] EC/DMC showed limited performance with NVPF-C (Figure S8e) presumably caused by water decomposition. The drying of $NaClO_4$

has been previously reported to cause technical difficulties due to its explosive nature.[59] The NVPF-C in 1 mol dm^{-3} $Na[ClO_4]$-PC shows a large capacity during the charge phase at 25 °C but failed to charge up to the upper cutoff voltage (4.3 V) at 45 °C and 60 °C (Figure S8f). The corresponding d*Q*/d*V* curves indicate two redox couples at about 3.7 V and 4.2 V caused by the (de)sodiation reactions of the Na^+ ions from Na (2) site and Na(1) sites, respectively, in NVPF-C at 25 °C (Figure S9a,d). On the other hand, severe oxidation peaks ascribed to electrolyte decomposition are observed above 45 °C and 60 °C (Figure S9b,e,c,f).

Among the organic electrolytes, the charge-discharge tests of NVPF-C in 1 mol dm^{-3} $Na[PF_6]$-EC/DMC presents the best results among the organic electrolytes (Figure 3a). Thus, further optimization was carried out by adding 3 wt% of FEC and 3 wt% of VC into 1 mol dm^{-3} $Na[PF_6]$-EC/DMC electrolyte. The results indicate that the addition of FEC or VC additives improves the charge-discharge behavior of the NVPF-C electrode even at 60 °C (Figure 3b,c). Table 1 lists the Coulombic efficiency of the first cycle in the series of electrolytes at 25 °C, 45 °C, and 60 °C. The first cycle Coulombic efficiencies are improved from 50.2% without additive, to 60.5% with FEC and 67.1% with VC at 60 °C. The ionic liquid electrolyte of 1 mol dm^{-3} Na[FSA]-$[C_3C_1pyrr][FSA]$ shows the highest first-cycle Coulombic efficiencies in this series across all the temperatures (88.6% at 25 °C, 84.8% at 45 °C, and 76.4% at 60 °C).

Figure 4 shows cycle performance of the NVPF-C electrode in the electrolytes; 1 mol dm^{-3} $Na[PF_6]$-EC/DMC + 3 wt% FEC or + 3 wt% VC and 1 mol dm^{-3} Na[FSA]-$[C_3C_1pyrr][FSA]$ exhibit relatively stable charge-discharge behavior in the first cycle up to 60 °C (Figure 3). Therefore, their cycle performance was evaluated over 500 cycles at temperatures of 25 °C and 60 °C as shown in Figure 4. Although the addition of FEC and VC additives into 1 mol dm^{-3} $Na[PF_6]$-EC/DMC allows cycling of the NVPF-C electrode, significant capacity degradation is observed throughout the cycling (Figure 4a). In both cases,

an increase in operating temperature improves the discharge capacity in the early cycles but leads to significant capacity drop after 300 cycles. The capacity retentions recorded after 500 cycles are 44.5%, 33.6% with FEC at 25 °C and 60 °C and 44.9%, and 33.8% with VC at 25 °C and 60 °C, respectively. Although average Coulombic efficiencies are at acceptable levels for 1 mol dm^{-3} Na[PF_6]-EC/DMC with FEC or VC additives, there are distinct fluctuations over the cycles with values reaching over 100% in some cases, suggesting unstable cycling behavior even in the presence of additives (Figure 4b). The results from LSV and charge-discharge tests, therefore, reveal that both FEC and VC can improve the oxidative stability of organic electrolytes but cannot reach satisfactory levels at elevated temperatures.

The NVPF-C cell using the 1 mol dm^{-3} Na[FSA]-[C_3C_1pyrr][FSA] achieved highly stable cyclability. The cycle performance was evaluated at a rate of 2C over 500 cycles at temperatures of 25 °C and 60 °C as shown in Figure 4. At 25 °C, very stable cycling performance at 25 °C observed, achieving outstanding capacity retention of 105.6% at the 500th cycle (vs. the 1st cycle) with a high average Coulombic efficiency of 99.8% throughout the 500 cycles. No fluctuation is observed. At 60 °C, the capacity gradually fades during cycling attaining capacity retention of 90.5% at the 500th cycle (vs. the 1st cycle) with an average Coulombic efficiency of 99.2% throughout the 500 cycles. This remarkable performance is attributed to the formation of a more robust CEI layer in the Na[FSA]-[C_3C_1pyrr][FSA] ionic liquid in comparison with the organic electrolytes. This could also explain the results from the XPS and EDX mapping later. However, when cycling was done at 90°C, faster capacity degradation is observed especially after 300 cycles. This temperature also produces the lowest Coulombic efficiency reaching 99.0% (**Figure S10**). This is an indicator that the CEI layer becomes unstable because temperature elevation triggers electrolyte decomposition leading to chemical reactions on the electrode surface during cycling. Cycling

performance at low temperatures of 0 °C and –20 °C were briefly investigated over 50 cycles (**Figure S11**). Although the cell exhibits limited performance at –20 °C, it retains a high reversible capacity of over 90 mAh g^{-1} at 0 °C. These electrochemical results show that the 1 mol dm^{-3} Na[FSA]-[C_3C_1pyrr][FSA] electrolyte can create and maintain a stable CEI layer even at lower operating temperatures.

2.2.2 Superior Electrochemical Performance Using Ionic Liquid Electrolytes over a Wide Temperature Range

Figure 5 shows the galvanostatic charge-discharge profiles of the NVPF-C electrode in 1 mol dm^{-3} Na[FSA]-[C_3C_1pyrr][FSA] over an operating temperature range of –20 °C to 60 °C. Reversible capacities of 121.0 mAh g^{-1}, 119.7 mAh g^{-1}, 102.4 mAh g^{-1} and 51.3 mAh g^{-1} are obtained at 60 °C, 25 °C, 0 °C and –20 °C, respectively. Although the polarization of charge-discharge curves becomes larger as the temperature decreases, the average discharge voltage of the NVPF-C electrode remains at 3.8 V at temperatures above 0 °C. **Table S5 s**hows that considerably high energy densities of 384 Wh Kg^{-1} and 206 Wh Kg^{-1} (based on positive electrode material alone) are still achieved even at the low temperatures of 0 °C and –20 °C, respectively (vs. an ideal Na metal negative electrode). The NVPF-C electrode delivers high rate performance across a wide temperature range (**Figure 6a-e**), demonstrating the possibility of application in extreme temperature environments.

To determine the kinetic characteristics underlying the improved electrochemical performance with temperature elevations, electrochemical impedance spectroscopic analysis (EIS) was performed as schematically shown in Figure 6f. Symmetric cells were adopted after adjusting the state of charge (SOC), and NVPF-C was also used as the counter electrode. Note here that half-cell configuration using sodium metal as a counter electrode, exhibits large

impedance, making it unsuitable for evaluation of the impedance information in sodium secondary battery target electrodes.[47, 60] Figure 6g shows the impedance Nyquist plots and fitted curves from the NVPF-C/NVPF-C symmetric cell (SOC = 50%). The equivalent circuit used to fit the plots is shown as the inset in Figure 6h, and the EIS parameters are provided in **Table S7**. The resistance at high-frequency regimes (R_1) is generally considered to emanate from the electrode-electrolyte interface of film resistance. In contrast, a resistance at low-frequency regimes (R_2) arises from charge-transfer resistance. The internal resistance of the electrode is represented as bulk resistance (R_{bulk}). Characteristic frequencies of these resistances shift to the high-frequency regimes with increasing operating temperatures. The reason behind the specific frequency shift is presumed to be a natural phenomenon and, to our knowledge, is not well established. The impedance values of R_{bulk}, $R_{1,}$ and R_2 decrease as the temperature increase, which shows an increase in Na^+ kinetics as manifested with improved rate performance at elevated temperatures. Furthermore, R_2 is more dependent on temperature than R_{bulk} and R_1. The attenuated rate performance at the temperature range of –20 °C to 25 °C is largely due to R_2, whereas at 60 °C it can be attributed to R_1. These results indicate that the charge-transfer resistance is the dominant factor that determines the rate capability of the NVPF-C electrode at low temperatures (below 25 °C), whereas at high temperatures (above 25 °C), there is cumulative involvement of R_{bulk}, R_1 and R_2. This observation is consistent with temperature dependence observed in some electrodes using ionic liquid electrolytes.[9, 60-64]

2.3 Thickness and Properties of CEI Layer

The characteristics of CEI components formed in the selected electrolytes at different temperatures were analyzed using XPS, and EDX mappings. **Figure 7** shows V *2p* XPS spectra of the NVPF-C electrode taken at different etching times (0 s, 10 s, 30 s and 60 s) after the

initial charging phase to the cut-off voltage of 4.3 V in the series of electrolytes at 25 °C and 60 °C (Figure 7a-d) and the corresponding V $2p_{3/2}$ peak (~ 517 eV) intensity profiles (Figure 7e,f). The thickness of the CEI is determined by evaluating the change in the intensity of the V $2p_{3/2}$. The peak intensity of V 2p decreases as the CEI becomes thicker. The results show a tendency of increasing CEI thickness as the operating temperature increases in any of the selected electrolytes. As the operating temperature increases, the solubility of the CEI components increases and becomes more unstable prompting electrolyte decomposition that increases the thickness of the CEI layer. The XPS spectra confirm charge-discharge measurement results indicating that NVPF-C in 1 mol dm^{-3} Na[PF_6]-EC/DMC develops a thicker CEI layer than in other electrolytes. The CEI layer decreases in thickness upon adding the FEC and VC additives into 1 mol dm^{-3} Na[PF_6]-EC/DMC, further confirming the profound effect additives have in the formation of a desirable CEI layer. The CEI layer formed in 1 mol dm^{-3} Na[FSA]-[C_3C_1pyrr][FSA] ionic liquid was the thinnest compared to the other electrolytes, affirming its excellent operation stability. This can be ascribed to the low solubility of electrolyte components of ionic liquids compared to organic electrolytes. These results are congruent with the results from the electrochemical performance test conducted in the previous sections.

More detailed XPS analyses were performed to further investigate the stability of the CEI constituents after initial charging of the NVPF-C electrode in 1 mol dm^{-3} Na[FSA]-[C_3C_1pyrr][FSA] to 4.3V. **Figure 8** shows Na 1s, F 1s, C 1s, O 1s, N 1s, P $2p_{3/2,}$ and P $2p_{3/2}$ XPS spectra of the NVPF-C electrode (see **Table S8** for further details relating to peak assignments). Moreover, EDX mappings were taken to clarify the chemical constituents at the surface of the NVPF-C electrode (see **Figure S12** for EDX mapping images and **Table S9** for elemental composition details). The EDX mapping reveals the CEI layer to be distributed

homogeneously over the surface of NVPF-C electrodes irrespective of the temperature. The increase in the elemental composition of sulfur (S) with an increase in operating temperatures coincides with a thicker CEI layer being formed at higher temperatures, as has been discussed in Figure 7. It is important to mention here that the presence of nitrogen (N)- and sulfur (S)-containing constituents may be a distinguishing factor between the CEI layers formed in Na[FSA]-[C_3C_1pyrr][FSA] ionic liquids from those of organic electrolytes based on $NaPF_6$-EC/DMC. In the ionic liquid, the main CEI constituents presumably arise from the oxidation of Na[FSA] (Na[$N(SO_2F)_2$]).[65, 66] The formation of NaF from Na^+ and decomposition of FSA^- is confirmed by the peaks at 1071.7 eV in Na 1s and 684.5 eV in F 1s. The N 1s, S $2p_{3/2}$, and O 1s spectra probably indicate the existence of amidyl radicals $^{\bullet}N(SO_2F)_2$, $–SO_x–$ (probably SO_2 and Na[SO_2F]), and C–N from the decomposition of the FSA^- and $C_3C_1pyrr^+$.[65-70] In addition, the C 1s peaks fitted at 284.4 eV, 285.4 eV, and 287.5 eV are assigned to C-C (C-H), C-O, and C=O, respectively.[71] The characteristic peaks of the CF_2 group in PVDF are observed at 290.2 eV and 687.5 eV in C 1s and F 1s, respectively, whereas the CH_2 group is at 284.4 eV in C1s.[52, 53, 72] The peak at 133.2 eV in P $2p_{3/2}$ is considered to be PO_4 in NVPF, as reported in the previous studies.[38]

3. Conclusion

In summary, the electrochemical stability of eleven organic solvent electrolytes and an ionic liquid were evaluated over a wide temperature range in an attempt to overcome the limited cyclability and Coulombic efficiency on the high-voltage positive electrode material, NVPF. Severe corrosion of Al occurs in Na[FSA]-based organic solvent electrolytes during the first charging step at all temperature variations due to poor stability. Without additives, Na[ClO_4] and Na[PF_6] based electrolytes decomposed at 45 °C and 60 °C. FEC and VC additives proved effective in improving the charge-discharge capacity and suppressing electrolyte degradation of the organic electrolytes. However, cycle deterioration was still prominent, resulting in low capacity retention (~44% at 25 °C and ~ 34% at 60 °C after 500 cycles). Ionic liquid: 1 mol dm^{-3} Na[FSA]-[C_3C_1pyrr][FSA] not only demonstrated excellent stability, but it also showed improved rate capability at elevated temperatures. The capacity retentions obtained after 500 cycles were 105.6% (average Coulombic efficiency: 99.8%) at 25 °C and 90.5% (average Coulombic efficiency: 99.2%) at 60 °C. The exceptional performance of the NVPF-C electrode in the ionic liquid electrolyte is a result of the thin and sturdy CEI layer arising from the oxidation of FSA^- in the ionic liquid electrolyte across the temperature range, as suggested by XPS and EDX analyses. This work clearly demonstrates the link between the formation of a stable CEI at high voltage regimes and the outstanding capabilities of ionic liquid electrolytes. It also highlights the functionality of ionic liquid electrolyte sodium batteries in severe temperature conditions.

Taming a high-voltage positive electrode is crucial in the pursuit of high energy batteries, especially sodium secondary batteries. This study opens new possibilities for research into CEI formation and characteristics as a way to maximize the potential of high-performance electrodes using ionic liquid electrolytes.

4. Experimental Section

General procedures and reagents

All air-sensitive materials were handled under dry Ar atmosphere in a glove box (H_2O < 1 ppm, O_2 < 1 ppm). Oxalic acid (Fujifilm Wako Pure Chemical Industries, purity > 98.0%), V_2O_5 (Sigma-Aldrich Chemistry, purity > 99.6%), NaF (Wako Pure Chemical Industries, purity > 97.0%), $NH_4H_2PO_4$ (Wako Pure Chemical Industries, purity > 99.0%), and glucose (Fujifilm Wako Pure Chemical Industries) was used as purchased. The salts, Na[FSA] (Mitsubishi Materials Electronic Chemicals, purity > 99%) and [C_3C_1pyrr][FSA] (Kanto Chemical, purity > 99.9%), $NaPF_6$ (Tokyo Chemical Industry, purity > 99%), and $NaClO_4$ (Fujifilm Wako Pure Chemical Industries, purity > 95.0%) were dried under vacuum for 24 h at 80 °C.

Preparation Procedures of NVPF-C

The NVPF-C composite was prepared via two-step synthesis, as shown in Figure S4. The carbon-coated VPO_4 (VPO_4-C) precursor was prepared through a sol-gel method. 1.8188 g (10.000 mmol) of V_2O_5 and 4.5015g (50.000 mmol) of oxalic acid was dissolved in the ion-exchange water at 80 °C while continuously stirring using a magnetic stirring bar coated with polytetrafluoroethylene (PTFE). 1.7115 g (9.4999 mmol) of glucose and 1.3001 g (19.999 mmol) $NH_4H_2PO_4$ were then added into the resulting solution and stirred for an additional 3 h. The oxalic acid and glucose were used as reducing agents and carbon sources, respectively. The solution was entirely dried at 120 °C and was then heated at 350 °C for 6 h and 700 °C for 8 h under Ar flow. After the heating process, the carbon content in VPO_4-C was determined to be 16.7% via combustion analysis. The prepared 2.466 g of VPO_4/C, and contained contains 2.1213 g (14.54 mmol) of VPO_4, was mixed with 0.9151 g (21.807 mmol) of NaF (2:3 molar ratio) and ball-milled (powder: ball = 1:10 in wt) for 1 h and heated once again at 700 °C for 8

h. The carbon content in the NVPF-C composite was 11.8% as was further determined by combustion analysis.

Preparation of Electrolytes

The Na[FSA]-based electrolytes, 1 mol dm^{-3} Na[FSA]-PC, 2 mol dm^{-3} Na[FSA]-PC, 1 mol dm^{-3} Na[FSA]-EC/DMC, and 2 mol dm^{-3} Na[FSA]-EC/DMC, were prepared by mixing Na[FSA] and PC (Kishida Chemical, H_2O < 30 ppm) or EC/DMC (1:1 v/v) (Kishida Chemical, H_2O < 30 ppm). The Na[ClO_4]- and Na[PF_6]-based electrolytes, 1 mol dm^{-3} Na[ClO_4]-EC/DMC, and 1 mol dm^{-3} Na[PF_6]-PC were prepared by mixing the corresponding salts and solvent in a target ratio. The 1 mol dm^{-3} Na[ClO_4]-PC (Kishida Chemical, battery grade) and 1 mol dm^{-3} Na[PF_6]-EC/DMC (1:1 in volume) (Kishida Chemical, battery grade) solutions were used as received. The additives, FEC (Fujifilm Wako Pure Chemical Industries) and VC (Fluorochem Ltd.), were used as received and added to 1 mol dm^{-3} Na[PF_6]-EC/DMC in 3 wt%. The ionic liquid electrolyte, 1 mol dm^{-3} Na[FSA]-[C_3C_1pyrr][FSA], was prepared by mixing Na[FSA] and [C_3C_1pyrr][FSA] and dried under vacuum for 24 h at 80 °C after mixing. The typical water content was below 30 ppm, according to Karl-Fischer titration (899 Coulometer, Metrohm).

Further experimental details

Details on material characterization, electrode and cell preparations, electrochemical measurements, and analytical results are summarized in the Supporting Information.

Supporting Information

Supporting Information can be found in the Wiley Online Library or directly from the author.

Acknowledgments

J. H. is grateful to the Japan Society for the Promotion of Science (JSPS) for the Grant-in-Aid for Scientific Research Fellowship. This study was conducted through the support of the Grant-in-Aid for Scientific Research grant program (19J14235) and the Japanese Ministry of Education, Culture, Sports, Science and Technology (MEXT) program "Elements Strategy Initiative to Form Core Research Center" (JPMXP0112101003).

Conflicts of Interest

The authors declare no conflict of interest.

Keywords

sodium secondary batteries, electrolytes, $Na_3V_2(PO_4)_2F_3$, wide operating temperature, ionic liquids

Received: ((will be filled in by the editorial staff))
Revised: ((will be filled in by the editorial staff))
Published online: ((will be filled in by the editorial staff))

The scarcity of electrolytes suitable for high voltage positive electrode materials such as $Na_3V_2(PO_4)_2F_3$, greatly undermines the implementation of sodium secondary batteries. In this study $Na_3V_2(PO_4)_2F_3$ performance is analyzed through screening of several organic and ionic liquid electrolytes. Results show the ionic liquid to be the most stable across a wide temperature range due to the formation of a CEI layer around the electrode.

sodium secondary batteries, electrolytes, $Na_3V_2(PO_4)_2F_3$, wide operating temperature, ionic liquids

Jinkwang Hwang, Kazuhiko Matsumoto, and Rika Hagiwara

Electrolytes Toward High-Voltage $Na_3V_2(PO_4)_2F_3$ Positive Electrode Durable Against Temperature Variation

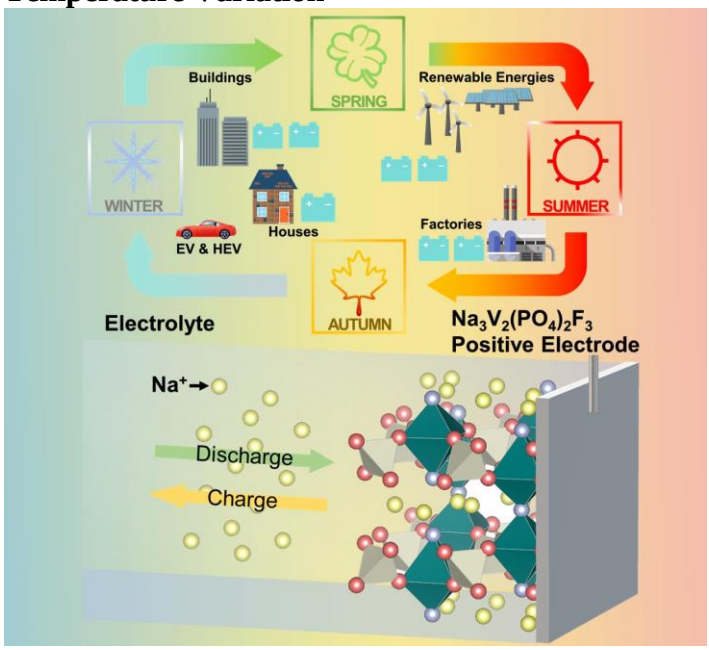

Table 1. Summary of the first cycle Coulombic efficiency of the NVPF-C electrode in various electrolytes.

Electrolytes	Temperature	First cycle Coulombic efficiency /%
	25 °C	Overcharged (Al dissolution)
1 mol dm^{-3} Na[FSA]-PC	45 °C	Overcharged (Al dissolution)
	60 °C	Overcharged (Al dissolution)
	25 °C	Overcharged (Al dissolution)
1 mol dm^{-3} Na[FSA]-EC/DMC	45 °C	Overcharged (Al dissolution)
	60 °C	Overcharged (Al dissolution)
	25 °C	Overcharged (Al dissolution)
2 mol dm^{-3} Na[FSA]-PC	45 °C	Overcharged (Al dissolution)
	60 °C	Overcharged (Al dissolution)
	25 °C	Overcharged (Al dissolution)
2 mol dm^{-3} Na[FSA]-EC/DMC	45 °C	Overcharged (Al dissolution)
	60 °C	Overcharged (Al dissolution)
	25 °C	56.4
1 mol dm^{-3} $Na[ClO_4]$-PC	45 °C	Overcharged (electrolyte decomposition)
	60 °C	Overcharged (electrolyte decomposition)
	25 °C	40.5
1 mol dm^{-3} $Na[ClO_4]$-EC/DMC	45 °C	29.4
	60 °C	Overcharged (electrolyte decomposition)
	25 °C	69.9
1 mol dm^{-3} $Na[PF_6]$-PC	45 °C	52.3
	60 °C	40.3
	25 °C	70.1
1 mol dm^{-3} $Na[PF_6]$-EC/DMC	45 °C	57.7
	60 °C	50.2
	25 °C	70.4
1 mol dm^{-3} $Na[PF_6]$-EC/DMC + 3wt% FEC	45 °C	68.7
	60 °C	60.5
	25 °C	75.4
1 mol dm^{-3} $Na[PF_6]$-EC/DMC + 3wt% VC	45 °C	72.4
	60 °C	67.1
	25 °C	88.6
1 mol dm^{-3} Na[FSA]-$[C_3C_1pyrr][FSA]$	45 °C	84.8
	60 °C	76.4

Table 2. Summary of cycle performance for NVPF-C in selected electrolytes.

Electrolytes	**Capacity retention (500th vs. 1st) / %**	**Average Coulombic efficiency (500 cylcles) / %**
1 mol dm^{-3} $Na[PF_6]$-EC/DMC + 3wt% FEC at 25 °C	44.5	97.8
1 mol dm^{-3} $Na[PF_6]$-EC/DMC + 3wt% FEC at 60 °C	33.6	94.3
1 mol dm^{-3} $Na[PF_6]$-EC/DMC + 3wt% VC at 25 °C	44.9	96.4
1 mol dm^{-3} $Na[PF_6]$-EC/DMC + 3wt% VC at 60 °C	33.8	87.7
1 mol dm^{-3} Na[FSA]-[C_3C_1pyrr][FSA] at 25 °C	99.9	99.8
1 mol dm^{-3} Na[FSA]-[C_3C_1pyrr][FSA] at 60 °C	90.5	99.2

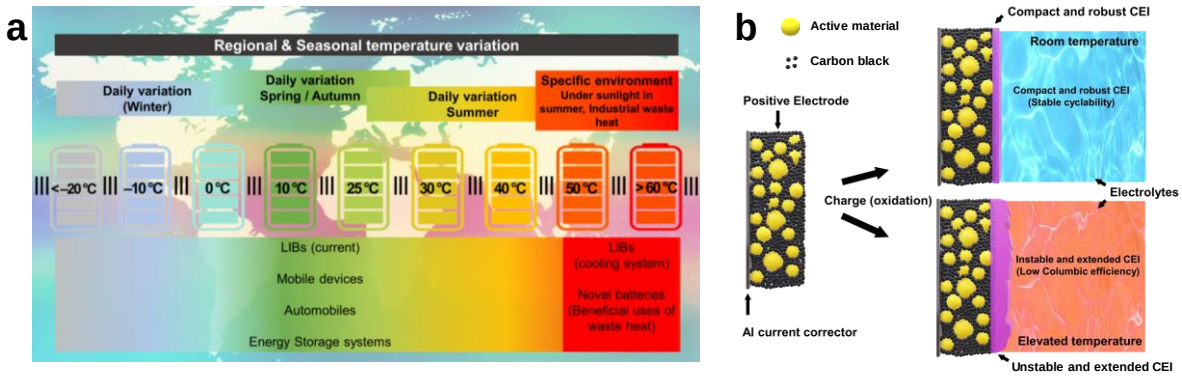

Figure 1. a) Operation temperature ranges of secondary batteries for selected applications and b) schematic drawing of difference in CEI formation depending on operating temperatures.

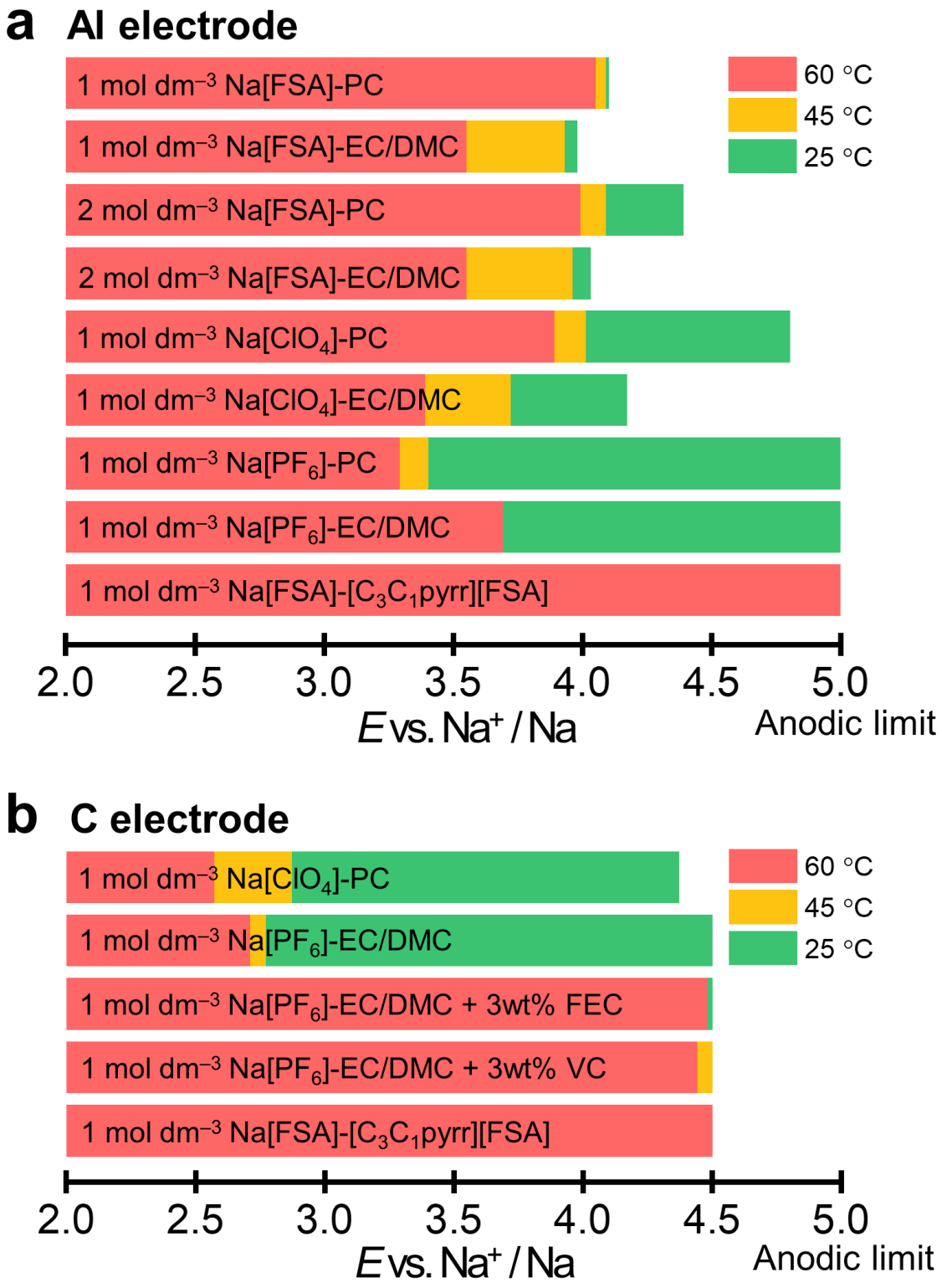

Figure 2. Anodic limits dependence on temperature for the electrolytes in this study. The anodic limits were determined by LSV on (a) Al and (b) C electrodes. The green, yellow, and red bars denote measurements at 25 °C, 45 °C, and 60 °C, respectively. See Figures S1 and S2 for the LSV data.

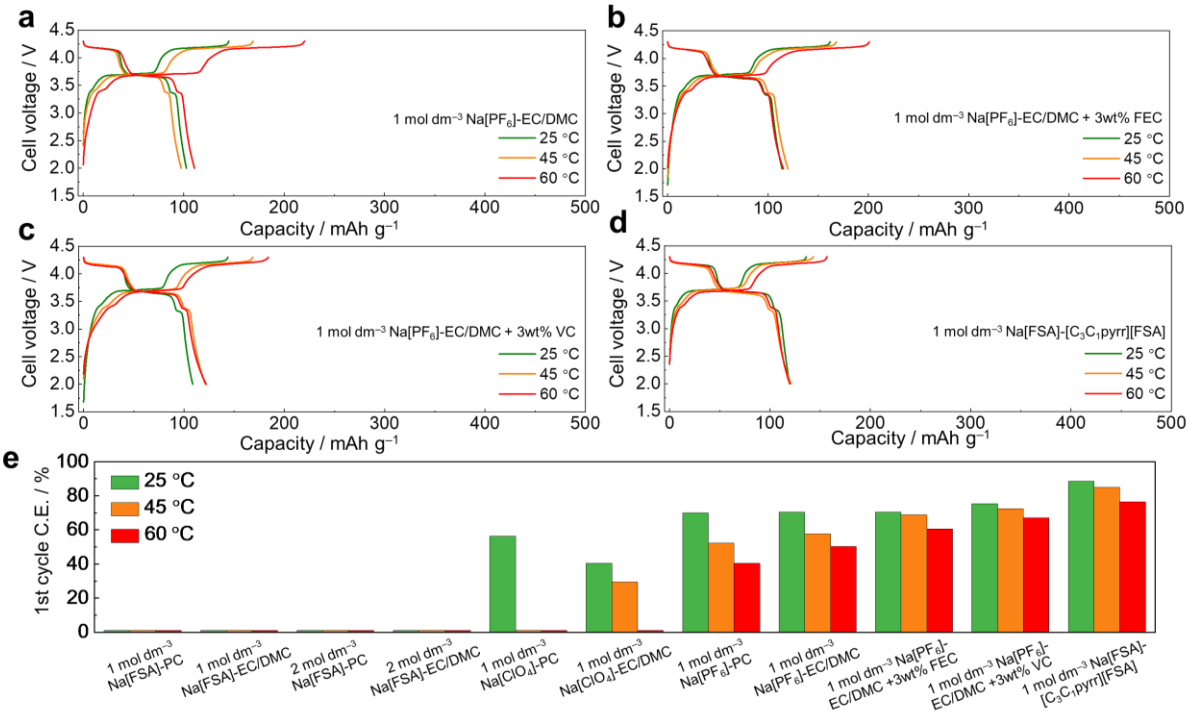

Figure 3. Charge-discharge curves of the NVPF-C electrode at 25°C, 45°C, and 60 °C for selected electrolytes. a) 1 mol dm^{-3} Na[PF_6]-EC/DMC, b) 1 mol dm^{-3} Na[PF_6]-EC/DMC + 3wt% FEC, c) 1 mol dm^{-3} Na[PF_6]-EC/DMC + 3wt% VC, and d) 1 mol dm^{-3} Na[FSA]-[C_3C_1pyrr][FSA]. e) The first cycle Coulombic efficiency for the electrolytes in this study measured at a C-rate of 0.1C and a cut-off voltage of 2.0 V/4.3 V. See Figure S8 for the charge-discharge curves of the NVPF-C electrode using other electrolytes, Table 1 for the Coulombic efficiency, and Figure S9 for the corresponding differential capacity dQ/dV plots.

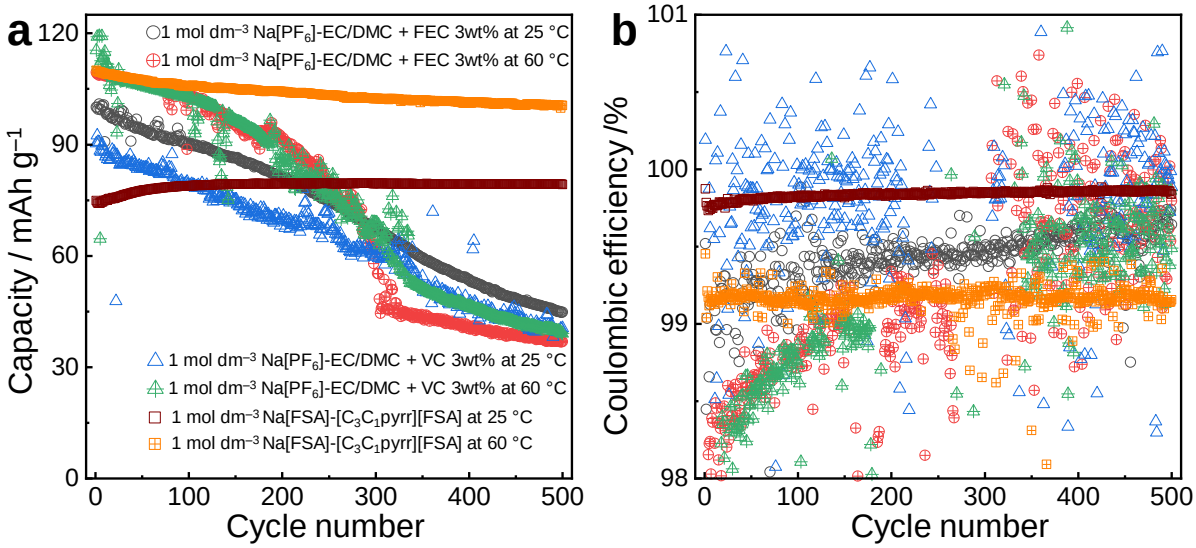

Figure 4. a) Cycle performance at 25 °C and 60 °C and b) the corresponding Coulombic efficiency plots of the NPVF-C electrode with the selected electrolytes measured at a C-rate of 2C and a cutoff voltage of 2.0 V/4.3 V. See Table 2 for cycle test details.

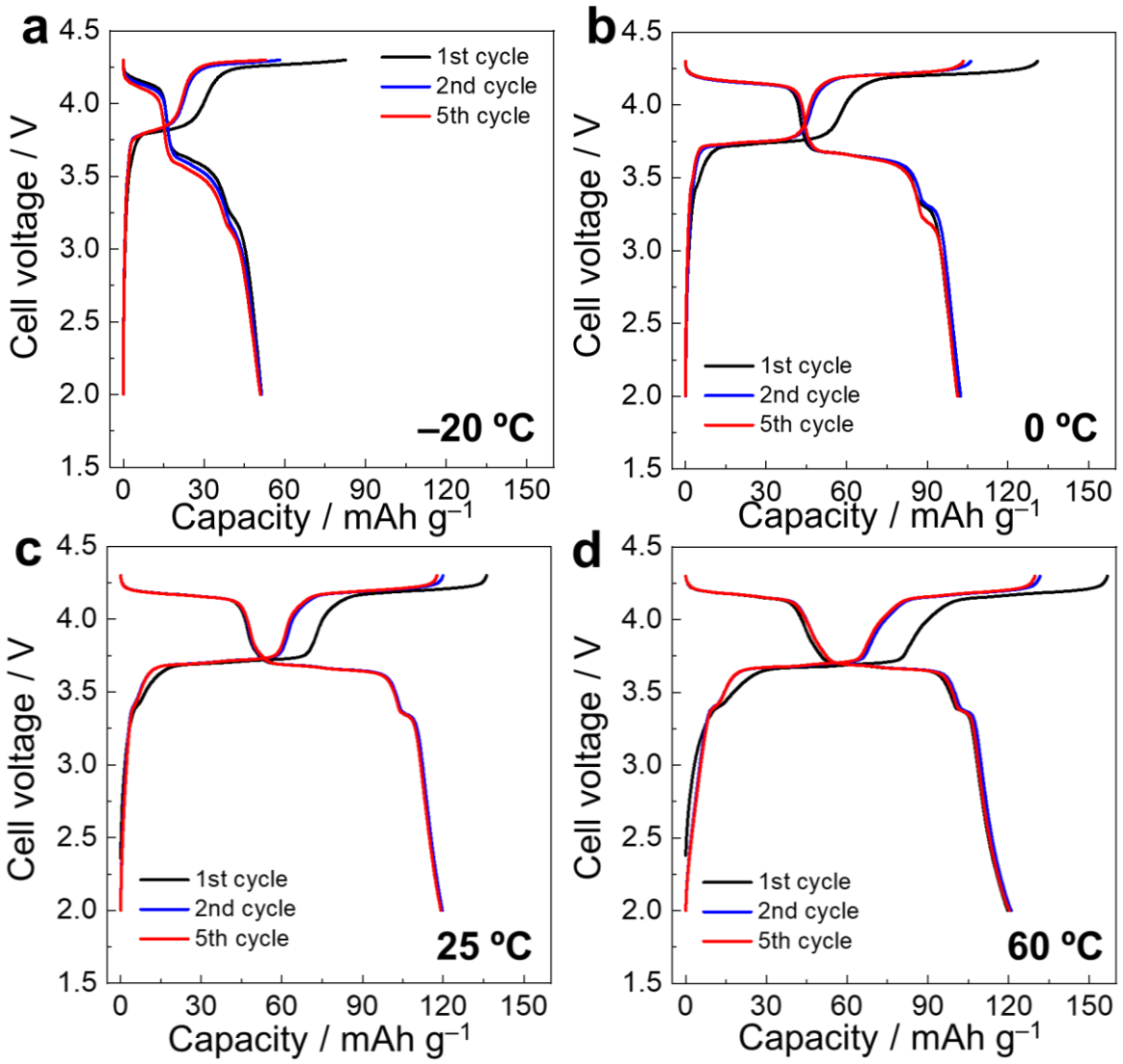

Figure 5. a-d) Charge-discharge curves of the NVPF-C electrode in 1 mol dm^{-3} Na[FSA]-[C_3C_1pyrr][FSA] measured at a C-rate of 0.1C and temperatures of a) –20 °C, b) 0 °C, c) 25 °C, and d) 60 °C.

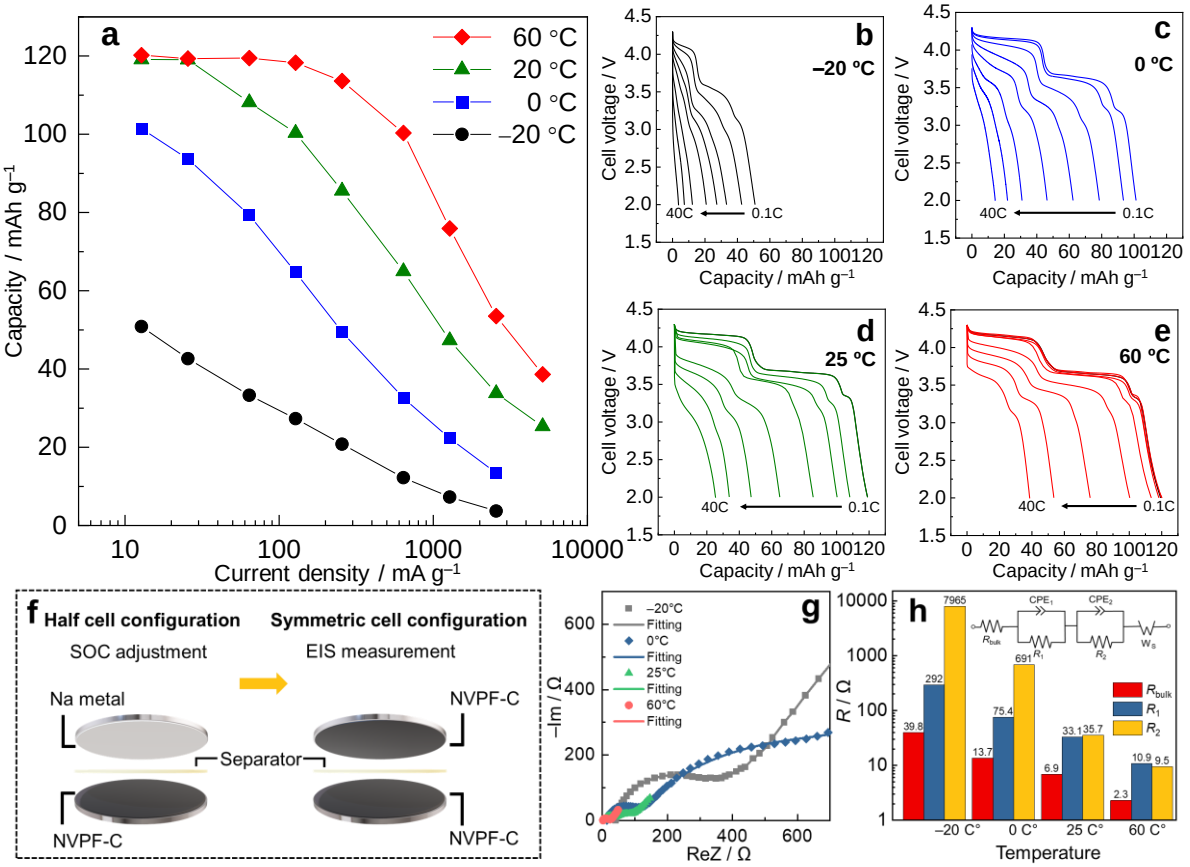

Figure 6. a) Rate capability dependence on temperature. b-e) Discharge curves of the NVPF-C electrode in the Na/1 mol dm^{-3} Na[FSA]-[C_3C_1pyrr][FSA] measured in the current density range of 0.1-40C at temperatures of a) –20 °C, b) 0 °C, c) 25 °C, and d) 60 °C. Cutoff voltage was set at 2.0 V/4.3 V. f) Schematic of a symmetric cell for EIS measurement. g) Nyquist plots and EIS fitting for the NVPF-C symmetric cells. SOC: 50%, AC perturbation: 10 mV, and frequency range: 100 mHz to 100 kHz. h) R_{bulk}, R_1, and R_2 obtained from EIS fitted plots. See Tables S5 and S6 for details of capacity, energy density, and capacity retention and Table S7 for EIS parameters.

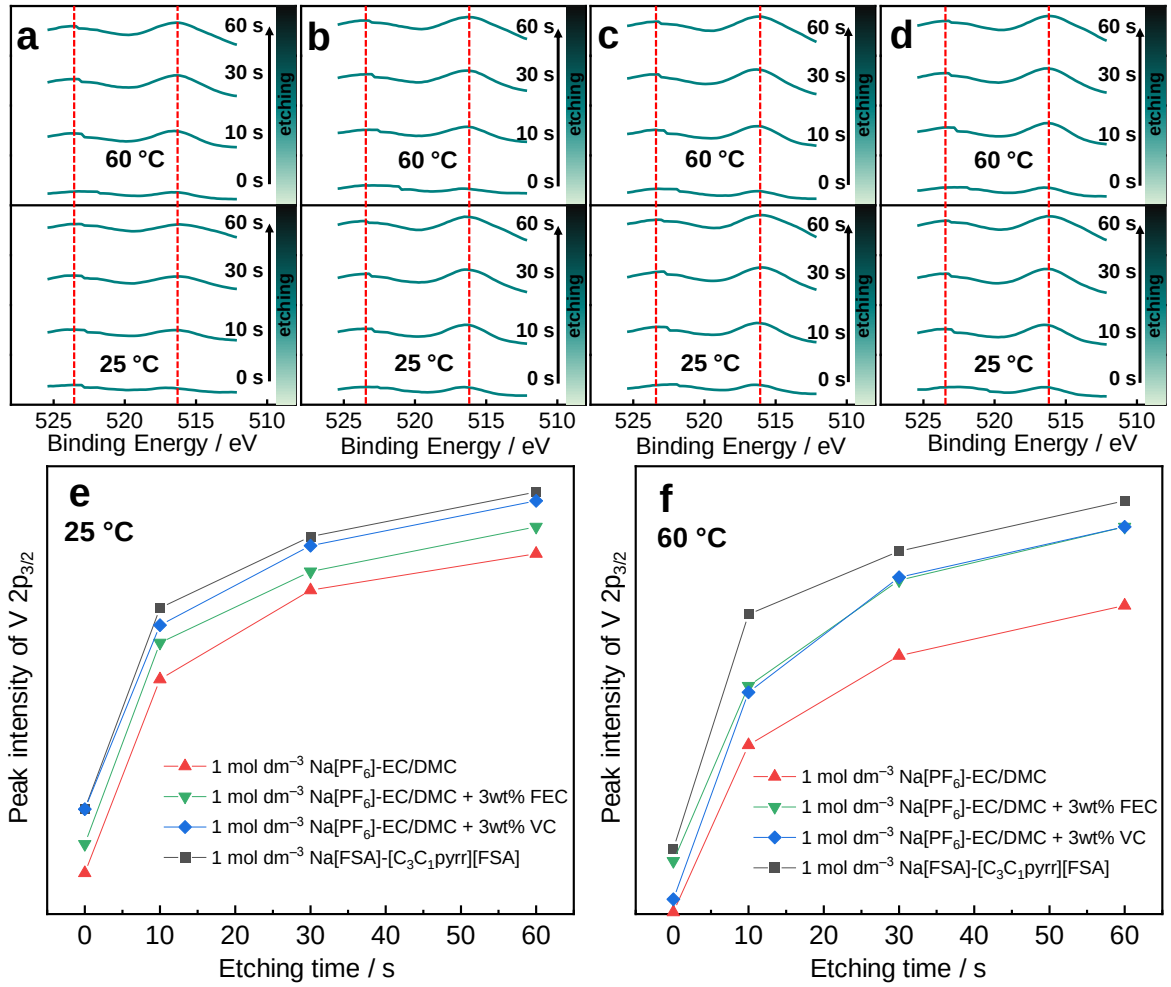

Figure 7. V $2p_{1/2}$ and V $2p_{3/2}$ XPS depth profiles for elements for NVPF-C electrode taken in a) 1 mol dm^{-3} $Na[PF_6]$-EC/DMC, b) 1 mol dm^{-3} $Na[PF_6]$-EC/DMC + 3wt% FEC, c) 1 mol dm^{-3} $Na[PF_6]$-EC/DMC + 3wt% VC, and d) 1 mol dm^{-3} Na[FSA]-$[C_3C_1pyrr][FSA]$. The peak intensity changes against etching time at e) 25 and f) 60 °C. Ar^+ sputtering power was set at 400 V.

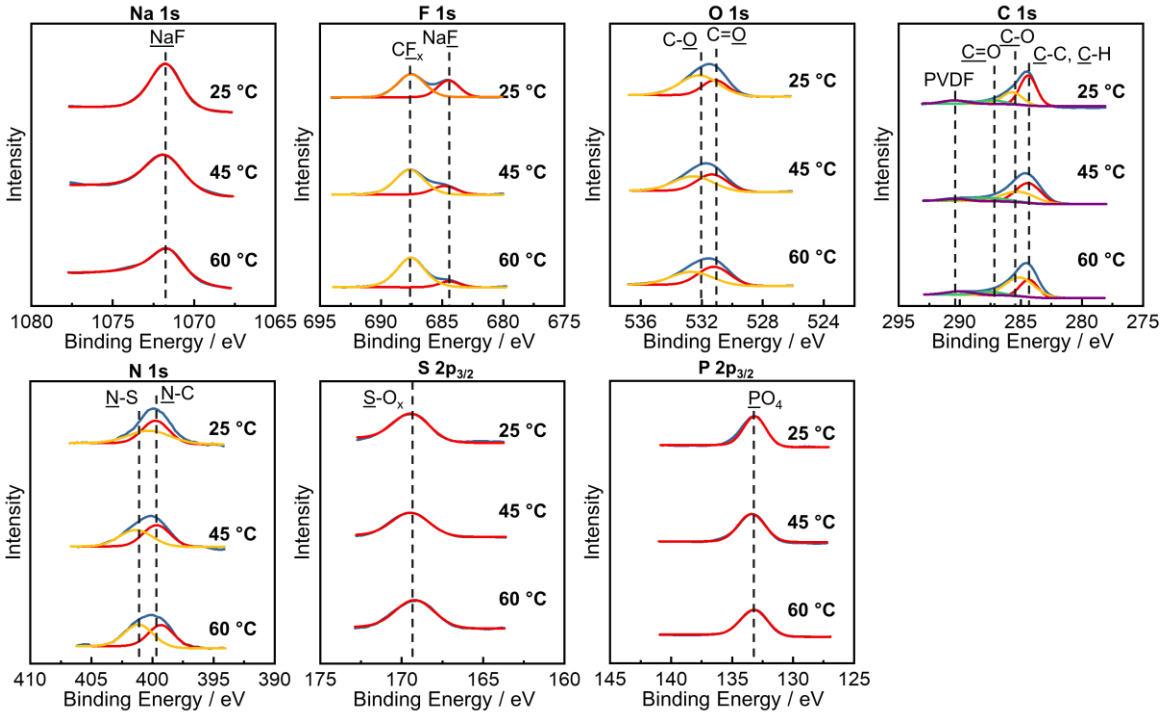

Figure 8. XPS spectra of the NVPF-C electrodes after the first charge in 1 mol dm^{-3} Na[FSA]-[C_3C_1pyrr][FSA] at 25, 45, and 60 °C; Na 1s, F 1s, O 1s, C 1s, N 1s, S $2p_{3/2}$, and P $2p_{3/2}$. See Table S8 for the binding energy of the peaks and CEI components.

References

[1] B. Dunn, H. Kamath, J.-M. Tarascon, *Science* **2011**, 334, 928.

[2] Y. Xiao, S. H. Lee, Y.-K. Sun, *Adv. Energy Mater.* **2017**, 7, 1601329.

[3] D. Larcher, J. M. Tarascon, *Nat. Chem.* **2015**, 7, 19.

[4] S. Chen, C. Wu, L. Shen, C. Zhu, Y. Huang, K. Xi, J. Maier, Y. Yu, *Adv. Mater.* **2017**, 29, 1700431.

[5] J.-M. Tarascon, *Nat Chem* **2010**, 2, 510.

[6] H. Vikstrom, S. Davidsson, M. Hook, *Appl. Energy* **2013**, 110, 252.

[7] K. Matsumoto, J. Hwang, S. Kaushik, C.-Y. Chen, R. Hagiwara, *Energy Environ. Sci.* **2019**, 12, 3247.

[8] D. R. MacFarlane, M. Forsyth, P. C. Howlett, M. Kar, S. Passerini, J. M. Pringle, H. Ohno, M. Watanabe, F. Yan, W. Zheng, S. Zhang, J. Zhang, *Nat. Rev. Mater.* **2016**, 1, 15005.

[9] J. Hwang, K. Matsumoto, R. Hagiwara, *Adv. Sustainable Syst.* **2018**, 2, 1700171.

[10] H. Zhang, I. Hasa, D. Buchholz, B. Qin, D. Geiger, S. Jeong, U. Kaiser, S. Passerini, *NPG Asia Mater.* **2017**, 9, e370.

[11] J. Hwang, K. Matsumoto, Y. Orikasa, M. Katayama, Y. Inada, T. Nohira, R. Hagiwara, *J. Power Sources* **2018**, 377, 80.

[12] C.-Y. Chen, T. Kiko, T. Hosokawa, K. Matsumoto, T. Nohira, R. Hagiwara, *J. Power Sources* **2016**, 332, 51.

[13] H. Usui, Y. Domi, H. Nishida, K. Yamaguchi, R. Yamagami, H. Sakaguchi, *ChemistrySelect* **2018**, 3, 8462.

[14] X. Lin, M. Salari, L. M. R. Arava, P. M. Ajayan, M. W. Grinstaff, *Chem. Soc. Rev.* **2016**, 45, 5848.

[15] D. R. MacFarlane, N. Tachikawa, M. Forsyth, J. M. Pringle, P. C. Howlett, G. D. Elliott, J. H. Davis, M. Watanabe, P. Simon, C. A. Angell, *Energy Environ. Sci.* **2014**, 7, 232.

[16] S.-W. Kim, D.-H. Seo, X. Ma, G. Ceder, K. Kang, *Adv. Energy Mater.* **2012**, 2, 710.

[17] N. Yabuuchi, K. Kubota, M. Dahbi, S. Komaba, *Chem. Rev.* **2014**, 114, 11636.

[18] V. Palomares, P. Serras, I. Villaluenga, K. B. Hueso, J. Carretero-González, T. Rojo, *Energy Environ. Sci.* **2012**, 5, 5884.

[19] M. D. Slater, D. Kim, E. Lee, C. S. Johnson, *Adv. Funct. Mater.* **2013**, 23, 947.

[20] H. Kim, H. Kim, Z. Ding, M. H. Lee, K. Lim, G. Yoon, K. Kang, *Adv. Energy Mater.* **2016**, 6, 1600943.

[21] P. R. Kumar, Y. H. Jung, C. H. Lim, D. K. Kim, *J. Mater. Chem. A* **2015**, 3, 6271.

[22] T. Broux, T. Bamine, F. Fauth, L. Simonelli, W. Olszewski, C. Marini, M. Menetrier, D. Carlier, C. Masquelier, L. Croguennec, *Chem. Mater.* **2016**, 28, 7683.

[23] M. Bianchini, F. Fauth, N. Brisset, F. Weill, E. Suard, C. Masquelier, L. Croguennec,

Chem. Mater. **2015**, 27, 3009.

[24] Q. Liu, D. Wang, X. Yang, N. Chen, C. Wang, X. Bie, Y. Wei, G. Chen, F. Du, *J. Mater. Chem. A* **2015**, 3, 21478.

[25] Y. Cai, X. Cao, Z. Luo, G. Fang, F. Liu, J. Zhou, A. Pan, S. Liang, J. Zhou, A. Pan, S. Liang, *Adv. Sci.* **2018**, 5, 1800680.

[26] Y.-U. Park, D.-H. Seo, H. Kim, J. Kim, S. Lee, B. Kim, K. Kang, *Adv. Funct. Mater.* **2014**, 24, 4603.

[27] K. Chihara, A. Kitajou, I. D. Gocheva, S. Okada, J.-i. Yamaki, *J. Power Sources* **2013**, 227, 80.

[28] W. Song, X. Cao, Z. Wu, J. Chen, Y. Zhu, H. Hou, Q. Lan, X. Ji, *Langmuir* **2014**, 30, 12438.

[29] W. Song, X. Ji, Z. Wu, Y. Yang, Z. Zhou, F. Li, Q. Chen, C. E. Banks, *J. Power Sources* **2014**, 256, 258.

[30] W. Song, Z. Wu, J. Chen, Q. Lan, Y. Zhu, Y. Yang, C. Pan, H. Hou, M. Jing, X. Ji, *Electrochim. Acta* **2014**, 146, 142.

[31] C. Zhu, C. Wu, C.-C. Chen, P. Kopold, P. A. van Aken, J. Maier, Y. Yu, *Chem. Mater.* **2017**, 29, 5207.

[32] B. Guo, W. Diao, T. Yuan, Y. Liu, Q. Yuan, G. Li, J. Yang, *J. Mater. Sci.: Mater. Electron.* **2018**, 29, 16325.

[33] C. Shen, H. Long, G. Wang, W. Lu, L. Shao, K. Xie, *J. Mater. Chem. A* **2018**, 6, 6007.

[34] H. Xiong, Y. Liu, Y. Yang, H. Shao, *J. Electrochem. Soc.* **2018**, 165, A746.

[35] J. Zhao, Y. Gao, Q. Liu, X. Meng, N. Chen, C. Wang, F. Du, G. Chen, *Chem. Eur. J.* **2018**, 24, 2913.

[36] L. Deng, G. Sun, K. Goh, L.-L. Zheng, F.-D. Yu, X.-L. Sui, L. Zhao, Z.-B. Wang, *Electrochim. Acta* **2019**, 298, 459.

[37] S. Liu, L. Wang, J. Liu, M. Zhou, Q. Nian, Y. Feng, Z. Tao, L. Shao, *J. Mater. Chem. A* **2019**, 7, 248.

[38] G. C. Yan, K. Reeves, D. Foix, Z. J. Li, C. Cometto, S. Mariyappan, M. Salanne, J. M. Tarascon, *Adv. Energy Mater.* **2019**, 9, 1901431.

[39] A. Ponrouch, R. Dedryvere, D. Monti, A. E. Demet, J. M. Ateba Mba, L. Croguennec, C. Masquelier, P. Johansson, M. R. Palacin, *Energy Environ. Sci.* **2013**, 6, 2361.

[40] R. Dugas, B. Zhang, P. Rozier, J. M. Tarascon, *J. Electrochem. Soc.* **2016**, 163, A867.

[41] S. Park, J. Song, S. Kim, B. Sambandam, V. Mathew, S. Kim, J. Jo, S. Kim, J. Kim, *Nano Res.* **2019**, 12, 911.

[42] T. Broux, F. Fauth, N. Hall, Y. Chatillon, M. Bianchini, T. Bamine, J.-B. Leriche, E. Suard, D. Carlier, Y. Reynier, L. Simonin, C. Masquelier, L. Croguennec, *Small Methods* **2019**, 3, 1800215.

[43] G. Yan, D. Alves-Dalla-Corte, W. Yin, N. Madern, G. Gachot, J.-M. Tarascon, *J. Electrochem. Soc.* **2018**, 165, A1222.

[44] S. Komaba, W. Murata, T. Ishikawa, N. Yabuuchi, T. Ozeki, T. Nakayama, A. Ogata, K. Gotoh, K. Fujiwara, *Adv. Funct. Mater.* **2011**, 21, 3859.

[45] D. I. Iermakova, R. Dugas, M. R. Palacín, A. Ponrouch, *J. Electrochem. Soc.* **2015**, 162, A7060.

[46] J. Hwang, K. Takeuchi, K. Matsumoto, R. Hagiwara, *J. Mater. Chem. A* **2019**, 7, 27057.

[47] X.-F. Luo, W.-H. Chiang, C.-Y. Su, T.-Y. Wu, S. B. Majumder, J.-K. Chang, *ACS Sustain. Chem. Eng.* **2019**, 7, 16682.

[48] J. Patra, H.-T. Huang, W. Xue, C. Wang, A. S. Helal, J. Li, J.-K. Chang, *Energy Storage Mater.* **2019**, 16, 146.

[49] G. G. Eshetu, S. Grugeon, H. Kim, S. Jeong, L. Wu, G. Gachot, S. Laruelle, M. Armand, S. Passerini, *ChemSusChem* **2016**, 9, 462.

[50] M. Forsyth, M. Hilder, Y. Zhang, F. Chen, L. Carre, D. A. Rakov, M. Armand, D. R. Macfarlane, C. Pozo-Gonzalo, P. C. Howlett, *ACS Appl. Mater. Interfaces* **2019**, 11, 43093.

[51] M. G. S. R. Thomas, P. G. Bruce, J. B. Goodenough, *Solid State Ionics* **1985**, 17, 13.

[52] J.-N. Zhang, Q. Li, Y. Wang, J. Zheng, X. Yu, H. Li, *Energy Storage Mater.* **2018**, 14, 1.

[53] G. Cherkashinin, K. Nikolowski, H. Ehrenberg, S. Jacke, L. Dimesso, W. Jaegermann, *Phys. Chem. Chem. Phys.* **2012**, 14, 12321.

[54] P. Peljo, H. H. Girault, *Energy Environ. Sci.* **2018**, 11, 2306.

[55] S.-T. Myung, Y. Hitoshi, Y.-K. Sun, *J. Mater. Chem.* **2011**, 21, 9891.

[56] J. W. Braithwaite, *J. Electrochem. Soc.* **1999**, 146, 448.

[57] J. Gaubicher, *J. Electrochem. Soc.* **1999**, 146, 4375.

[58] L. Otaegui, E. Goikolea, F. Aguesse, M. Armand, T. Rojo, G. Singh, *J. Power Sources* **2015**, 297, 168.

[59] A. Ponrouch, D. Monti, A. Boschin, B. Steen, P. Johansson, M. R. Palacín, *J. Mater. Chem. A* **2015**, 3, 22.

[60] J. Hwang, K. Matsumoto, R. Hagiwara, *J. Phys. Chem. C* **2018**, 122, 26857.

[61] C.-Y. Chen, T. Kiko, T. Hosokawa, K. Matsumoto, T. Nohira, R. Hagiwara, *J. Power Sources* **2016**, 332, 51.

[62] S. Kaushik, J. Hwang, K. Matsumoto, Y. Sato, R. Hagiwara, *ChemElectroChem* **2018**, 5, 1340.

[63] J. Hwang, K. Matsumoto, Y. Orikasa, M. Katayama, Y. Inada, T. Nohira, R. Hagiwara, *J. Power Sources* **2018**, 377, 80.

[64] J. Hwang, K. Matsumoto, R. Hagiwara, *ACS Appl. Energy Mater.* **2019**, 2, 2818.

[65] I. A. Shkrob, T. W. Marin, Y. Zhu, D. P. Abraham, *J. Phys. Chem. C* **2014**, 118, 19661.

[66] A. Basile, A. I. Bhatt, A. P. O'Mullane, *Nat. Commun.* **2016**, 7, 11794.

[67] H. Usui, Y. Domi, R. Yamagami, K. Fujiwara, H. Nishida, H. Sakaguchi, *ACS Appl. Mater. Interfaces* **2018**, 1, 306.

[68] M. Dahbi, M. Fukunishi, T. Horiba, N. Yabuuchi, S. Yasuno, S. Komaba, *J. Power Sources* **2017**, 363, 404.

[69] Q. Zheng, Y. Yamada, R. Shang, S. Ko, Y.-Y. Lee, K. Kim, E. Nakamura, A. Yamada, *Nat. Energy* **2020**.

[70] J.-S. Kim, H. Choi, J.-N. Lee, H. Kang, D. Im, H. Kim, *RSC Advances* **2017**, 7, 24679.

[71] L.-L. Zhang, D. Ma, T. Li, J. Liu, X.-K. Ding, Y.-H. Huang, X.-L. Yang, *ACS Appl. Mater. Interfaces* **2018**, 10, 36851.

[72] Y. Sato, K. Itoh, R. Hagiwara, T. Fukunaga, Y. Ito, *Carbon* **2004**, 42, 3243.